# Damping of phonons in one-dimensional quantum fluids

Federica Cataldini,<sup>1</sup> Nataliia Bazhan,<sup>1</sup> João Sabino,<sup>1</sup> Philipp Schüttelkopf,<sup>1</sup> Mohammadamin Tajik,<sup>1,\*</sup> Frederik S. Møller,<sup>1,2</sup> Si-Cong Ji,<sup>1</sup> Sebastian Erne,<sup>1</sup> Igor Mazets,<sup>1</sup> and Jörg Schmiedmayer<sup>1</sup>

<sup>1</sup>Vienna Center for Quantum Science and Technology (VCQ), Atominstitut, TU Wien, Vienna, Austria

<sup>2</sup>Institute of Science and Technology Austria, 3400 Klosterneuburg, Austria

(Dated: November 18, 2025)

Collective excitations in one-dimensional (1D) quantum fluids are expected to propagate almost without dissipation. Here we directly excite phonon modes in a weakly interacting 1D Bose gas and study their time evolution. In the linear response regime, damping is surprisingly fast and quantitatively follows the non-analytic scaling  $\Gamma_k \propto k^{3/2}$  predicted by Andreev's hydrodynamic description. For stronger excitations, we observe a crossover to a highly nonlinear regime characterized by wave breaking, captured by the finite-temperature nonlinear Schrödinger evolution. Our results resolve a long-standing question on the fate of phonons in 1D Bose gases, and open new pathways to study non-linear relaxation in quantum many-body systems.

One-dimensional (1D) quantum systems have long served as paradigms of analytically tractable many-body physics. Since the seminal works of Girardeau, of Lieb and Liniger, and of Haldane [1-4], they have provided exact models in which interactions, quantum statistics, and dimensionality intervene in non-trivial ways. Their theoretical framework, from bosonization to nonlinear Luttinger-liquid and hydrodynamic descriptions, is now well established and comprehensively reviewed in Refs. [5-9]. With the advent of ultracold-atom experiments, these concepts became directly testable, enabling quantitative studies of non-equilibrium dynamics and integrability. Landmark experiments, including the quantum Newton's cradle [10], pre-thermalization [11], long-time recurrences [12], and the controlled tuning of dipolar interactions [13], have revealed how coherence and relaxation emerge even in isolated 1D quantum fluids.

The bosonization framework [4–7] captures dynamics in 1D quantum systems in terms of collective bosonic modes—phonons. In the long-wavelength limit  $(k \to 0)$ , the excitation spectrum is linear,  $\omega_k = ck$ , where  $k, \omega_k$ , and c are the wave number of an excitation, its frequency, and the speed of sound, respectively, and the resulting Tomonaga–Luttinger liquid describes a perfectly coherent, integrable fluid in which these phonons are non-interacting and possess infinite lifetimes. Real systems, however, inevitably deviate from this idealization. Band-curvature effects lead to phonon decay and spectral broadening, giving rise to the nonlinear Luttinger-liquid (NLL) framework [8, 14, 15], where the dynamical structure factor  $S(k,\omega)$  acquires universal power-law edge singularities governed by the Luttinger parameter K.

A complementary picture is offered by Andreev's hydrodynamic treatment [16]. It treats the decay rate  $\Gamma_k$  of a density-phase wave self-consistently and predicts a non-analytic k-dependence,  $\Gamma_k \propto k^{3/2}$ , for long-wavelength phonons. In this view, the decay of the coherent amplitude of a density perturbation reflects the collective, temperature-dependent scattering of sound waves rather than single-particle collisions—a regime our experiment now accesses directly.

Long-wavelength phonons acquire a finite lifetime through resonant branching (phonon with wave number k can decay

into two phonons with wave numbers  $k_1$  and  $k_2 = k - k_1$ ) and merging processes ( $k_1$  and  $k_2$  merge into a phonon with  $k = k_1 + k_2$ ) that satisfy energy and momentum conservation for all intermediate wave numbers. Solving this problem in the single-pole approximation for the phonon Green's function yields an exponential decay of the mode amplitude with a universal, non-analytic damping rate

$$\Gamma_k = \alpha \sqrt{\frac{k_B T}{m n_{1D}}} k^{3/2},\tag{1}$$

where  $k_B$  is the Boltzann constant, T is the temperature, m the atomic mass,  $n_{1D}$  the linear density, and  $\alpha \approx 1$  a dimensionless constant. Remarkably, the sound velocity c enters only implicitly through the regime of validity  $\hbar k \lesssim mc$ . Our work provides the first direct experimental confirmation of this universal prediction by measuring the lifetime of phonons in a weakly interacting quasi-1D Bose gas of ultracold  $^{87}{\rm Rb}$ 

Equation (1) arises from a hydrodynamic description that represents the classical (mean-field) limit of the Lieb-Liniger model [2], formulated in terms of conjugate phase and density variables [17]. In this regime, the relevant excitations are long-wavelength phonons whose mutual interactions are captured by a self-consistent classical field theory. The underlying mechanism is thus much simpler than in the nonlinear Luttinger-liquid (NLL) framework [14, 15], where the relevant bosonic quasiparticles emerge as composite pairs of Lieb-Liniger particle- and hole-type excitations with distinct dispersion relations. It also differs from integrability-breaking mechanisms arising from density-dependent transverse confinement effects [18, 19], which in the semiclassical limit are described by the non-polynomial Schrödinger equation (NPSE) [20]. Crucially, the finite damping rate  $\Gamma_k \propto k^{3/2}$ predicted by Eq. (1) remains fully compatible with the integrability of the classical mean-field limit [21]: numerical studies have shown that while phonon populations relax toward stationary distributions, the underlying integrals of motion remain conserved [22].

Direct experimental confirmation of this universal damping  $\Gamma_k \propto k^{3/2}$  has so far remained out of reach. Earlier

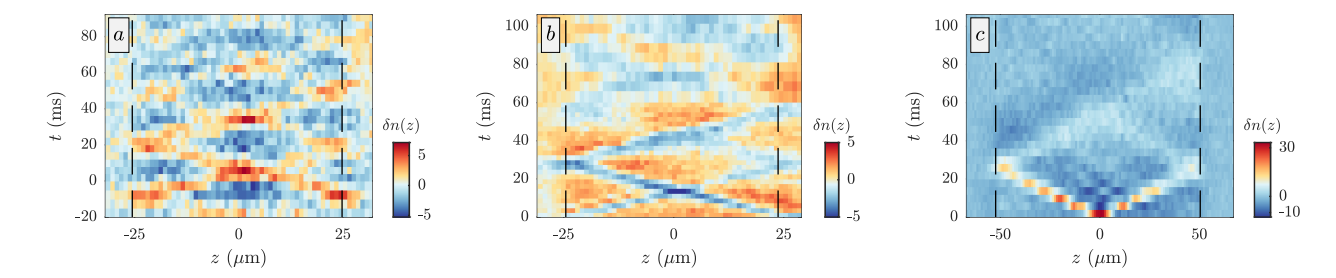


FIG. 1. **Density perturbation dynamics.** Time evolution of three distinct density perturbations: second mode excited via shaking of the box walls (a), density wave packets emerging from ramping down the potential amplitude in 1 ms (b), density wave packets emerging after quenching a potential with central dimple to a flat box (c). The x-axis corresponds to the longitudinal direction z, while the y-axis shows the evolution time. For panel (a) negative times indicates the driving time, while t > 0 always represent free dynamics. The position of the box walls during the free evolution is shown with dashed lines. The colorbar indicates the amplitude of the perturbation. The inital temperature for the three datasets is 64 (11), 40 (4) and 69 (5) nK, respectively, while the linear density is 73, 78 and  $68 \mu m^{-1}$ 

work on coherently split 1D Bose gases observed indirect evidence through a subexponential decay of the interference contrast,  $\propto \exp[-(t/t_0)^{2/3}]$  [23], shown theoretically [24, 25] to be consistent with ensemble-averaged phonon damping governed by Eq. (1). However, such global coherence measurements probe the collective dynamics of many modes rather than the lifetime of a single, well-defined phonon. The ability to resonantly excite and track the evolution of a single phononic mode, leaving the thermal background essentially unperturbed, has therefore represented a key experimental challenge, and forms the central advance of the present work.

Here, we overcome this challenge by resonantly driving individual phonon excitations in a quasi-1D Bose gas and tracking the evolution of their coherent amplitude in time. This approach provides a direct test of Eq. (1) and offers a new window into the microscopic decoherence mechanisms in low-dimensional quantum fluids. In addition, we implement three distinct protocols to initiate wave packet propagation in the Bose gas, allowing us to collectively excite low-momentum phononic modes over a wide range of perturbation amplitudes. This reveals a crossover from a regime dominated by phonon–phonon scattering to a highly nonlinear regime, characterized by wave-breaking dynamics.

In our setup, the quasi-condensate is prepared on an atom chip [26], where a cigar-shaped magnetic trap is overlaid with an optical dipole potential that defines the geometry of the system in the longitudinal direction. The experiments are carried out in a box-shaped trap that discretizes the allowed wave number as  $k=\frac{\pi}{L}j$ , where L is the system size and  $j=1,2,3,\ldots$  labels the mode number. The box trap is realized by shining a blue-detuned laser beam onto an opaque mask, aligned parallel to the longitudinal axis of the atomic cloud, thereby creating two hard walls on the underlying shallow harmonic confinement (refer to Section A of the Supplemental material for more details).

To resonantly excite the  $j^{th}$  phononic mode, we continuously modulate the intensity of the dipole beam at frequency  $\omega_{k_j}$  and monitor the system's response through the density perturbation profile recorded at discrete times. The density perturbation can be expressed as the sum of cosine

modes  $\delta n(z,t) = \sum_{i=1}^{\infty} \delta \tilde{n}_i(t) \cos(k_i z)$ , with  $\delta \tilde{n}_i(t)$  the time-dependent amplitude of the  $i^{th}$  mode. Under resonant driving, only the targeted mode contributes significantly to  $\delta n(z,t) \approx \delta n_j(t) \cos(k_j z)$ .

A representative experiment is shown in Fig.1(a), where the  $2^{nd}$  mode is excited, yielding  $\delta n(z,t)=\delta n_2(t)\cos((2\pi z)/L).$  Given the symmetry of the external trapping potential and of the driving protocol only even modes can be excited; hence the  $2^{nd}$  mode is the lowest we can access. In the figure, we show the last  $20\,\mathrm{ms}$  of driving and the subsequent evolution for  $100\,\mathrm{ms}.$  At each time step, we record a statistically significant set of absorption images after a  $2\,\mathrm{ms}$  time-of-flight (ToF) expansion, from which we extract the averaged density profile n(z,t). The density perturbation is defined as  $\delta n(z,t)=n(z,t)-\langle n(z,t)\rangle_t,$  where  $\langle\cdot\rangle$  denotes the average over time.

All single mode measurements presented are performed in a box of length  $L \simeq 49\,\mu m$ , linear density  $n_{1D} \in [60-75]\,\mu m^{-1}$  and initial temperature  $T \in [50-65]\,n K$ , deep in the 1D regime [27, 28]. The perturbation amplitude is about  $\delta n/n_{1D} \in [0.04, 0.06]$  of the linear density.

The damping rate of each excited mode is extracted through a Fourier analysis of the resulting density perturbation carpet (Fig.1(a)). Specifically, for each recorded evolution time, we compute the Fourier transform of the perturbation profile  $\delta n(z)$ . To avoid boundary effects, the operation is conducted within the internal part of the box, specifically in the region between the vertical dashed lines, as marked in Fig. 1 and Fig. 4(a). The panel (b) of Fig. 2 shows the mode decomposition for the measurement presented in Fig. 1(a). We find that only the excited mode is significantly populated and its amplitude  $\delta \tilde{n}_2(t)$  evolves following a damped oscillation (Fig. 2(f)), whereas the amplitude of higher modes is negligible, demonstrating that we can excite a single phononic mode with great accuracy.

In addition to the  $2^{nd}$  mode we are able to excite the next three symmetric modes (see Fig 5 of SM), thus spanning a large interval of k-space. The mode decomposition for measurements where the  $4^{th}$ ,  $6^{th}$  and  $8^{th}$  are excited is shown in Fig.2(c-e). We observe that the phonons' lifetime  $\tau = \Gamma^{-1}$ 

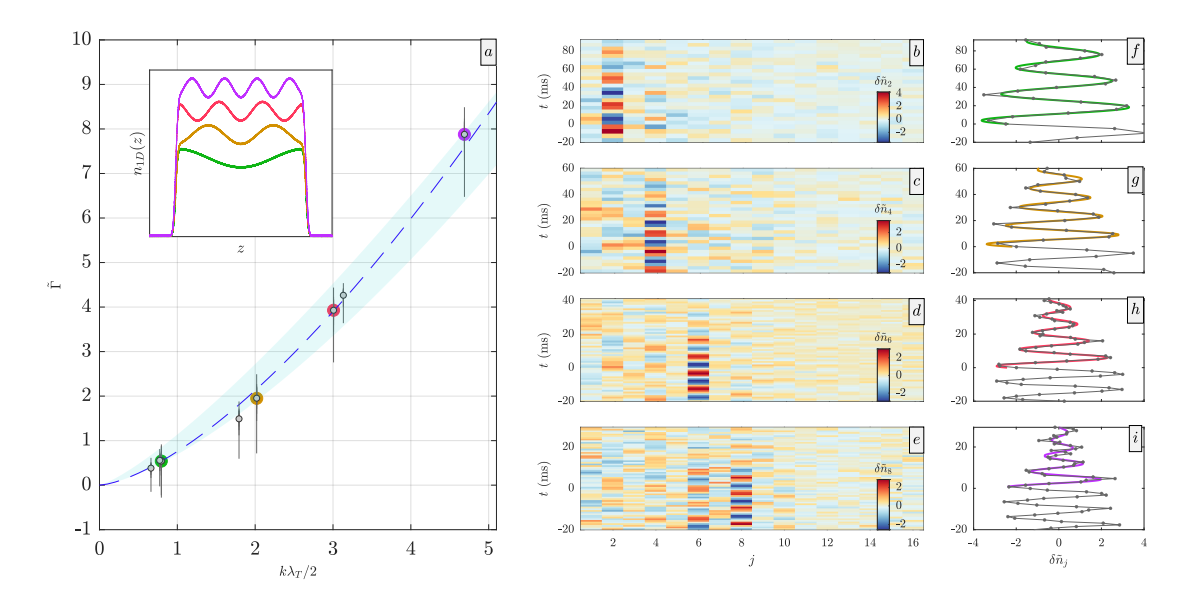


FIG. 2. Damping extracted from single mode dynamics. (a): Behaviour of the normalized damping rate  $\tilde{\Gamma}=(m\lambda_T^2\Gamma)/(4\hbar)$  at different k. Experimental data are shown with dots, with errorbars indicating the 68% confidence interval, computed via bootstrap. The dashed line is the curve obtained with fitted coefficient  $\alpha=0.76~(0.02)$  and fitted exponent  $\beta=1.48~(0.03)$ , where the errors correspond to two standard deviations (see Supplemental material). The shaded area represents the NPSE simulation of experimental data, taking into account uncertainty on  $\tilde{\Gamma}$  due to temperature variation and perturbation amplitude. Four experimental data sets with distinct  $k_j$  are highlighted in different colors, and their schematic density profile is shown in the inset of panel (a). Mode j=2,4,6,8 are indicated with green, orange, red and purple, respectively. (b-e): Mode decomposition of the selected data sets. On the x-axis is the mode number j and on y-axis is time. Negative values indicate the driving time  $\tau_{dr}$ ; at t=0 the modulation is turned off, followed by the free evolution in the box for t>0. (f-i): Full evolution of the addressed mode at a fixed k:  $k_2=2\pi/L$ ,  $k_4=4\pi/L$ ,  $k_6=6\pi/L$ ,  $k_8=8\pi/L$ , respectively. The driving time for the four data sets is  $\tau_{dr}=60,45,60$  and 40 ms, respectively. Of the full driving time only the last 20 ms are showed in the plots.

decreases for higher-order modes, and it can be extracted by fitting  $\delta \tilde{n}_j$  with the function:

$$f(t) = A_0 \exp(-t/\tau) \cos(\omega_k t + \phi), \tag{2}$$

where  $A_0$ ,  $\omega_k$  and  $\phi$  are the other fitting parameters, representing the initial amplitude of the mode, oscillation frequency, and initial phase, respectively.

To explore the k-dependence of the damping, we analyze eight independent measurements, each addressing one of the four lowest modes, and extract the corresponding damping rate. Since the measurements were performed under slightly different experimental conditions, specifically, variations in box length and initial temperature, we compare them in Fig. 2(a) using normalized quantities, allowing for a direct and consistent comparison across data sets: We use  $\tilde{\Gamma}=\frac{m}{\hbar}\frac{\lambda_T^2}{4}\Gamma$  and  $\tilde{k}=k\frac{\lambda_T}{2}$ , with m atomic mass of  $^{87}$ Rb atoms and  $\lambda_T=(2\hbar^2n_{1D})/(mk_BT)$  thermal coherence length. By fitting the extracted damping with an power-law function (shown as a dashed line), we find that both the exponent and the prefactor are in excellent quantitative agreement with Andreev's hydrodynamic theory [16]. In particular, we fit the coefficient  $\alpha = 0.76 \, (0.02)$  and the exponent  $\beta = 1.48 \, (0.03)$ . This result establishes phonon-phonon scattering as the dominant relaxation channel in weakly interacting one-dimensional Bose gases. Importantly, the self-consistent approach [16], predicting non-analytic behavior  $\Gamma_k \propto k^{3/2}$  as  $k \to 0$ , is in clear contrast to the treatment applicable to higher dimensions [29, 30].

The second approach we use to investigate the out-of-equilibrium dynamics of excitations is to initiate the propagation of wave packets into the system, which excites several modes at the same time, each with frequency given by the dispersion relation  $\omega_j=(\pi/L)j$ , where j=1,2,...,J and J is the highest mode we can detect given our imaging resolution. In our setup, the imaging resolution in the longitudinal direction is about  $1\,\mu m$ , hence it becomes hard to detect modes whose frequency  $\omega/(2\pi)\gtrsim 170\,$  Hz. To investigate the dynamics of wave packets we implement three different protocols which allow us to greatly vary the perturbation amplitude, ranging from 5% up to 40% of the background density.

The low amplitude regime is investigated by ramping up or down the box potential by a small quantity  $V_{box}(t>0)=V_{box}(t=-t_r)\pm\delta V_{box}$ , where  $t_r=1\,ms$  is the short ramping time,  $V_{box}(t=-t_r)$  is the potential at the thermal state and  $\delta V$  is the small potential variation (see Fig. 3(f)). An experiment where such protocol is applied is shown in Fig. 1(b), where a perturbation amplitude of about 5% of the linear density  $n_{1D}=78~\mu m^{-1}$  is achieved. Its mode decomposition is plotted in Fig.3b).

A different protocol is used for the experiment shown in Fig. 4(a), whose mode decompostion is plotted in Fig. 3(c). Here we initiate wave packets by slightly shrinking the box (see Fig. 3(g)): the box edges are shifted by  $\Delta L \sim 2 \, \mu m$  each in  $t_s = 5 \, ms$ :  $L(t>0) = L(t=-t_s) - 2 \Delta L$  (more details are provided in section B of the SM). As the walls of the box get displaced, the atoms on the side are

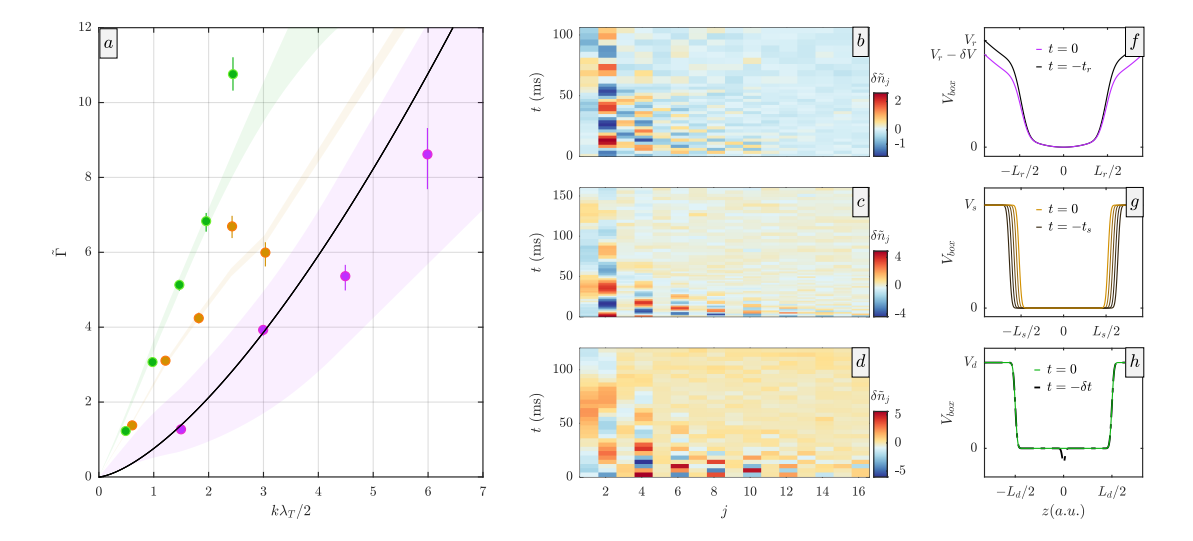


FIG. 3. Damping extracted from wave packets dynamics. Panel a): behaviour of  $\tilde{\Gamma}$  for different k. Data points of the same color represent the lower modes excited through different protocols: in magenta are the data obtained via a fast ramp in the box trap and their mode decompostion shown in panel b); in orange are the data obtained by symmetric box walls displacement, while in green are modes excited after quenching a dimple potential to a flat box. The mode decompostion for the orange and green data set are displayed in panel c) and d), respectively. The correspondent evolution of the density perturbation in real space is show in Fig.1b), Fig. 4a) and Fig.1c). The black solid line is the expected Andreev damping obtained with coefficient  $\alpha=0.76$  as obtained from the fit of the shaking measurements (Fig. 2a)). The shaded areas represent finite temperature NPSE simulations of experimental data, taking into account uncertainty on temperature and on perturbation amplitude. Panels f) to h): Schematic illustration of the three protocols; relative proportions are not to scale.

pushed to the center, giving rise to two wave packets, left (L) and right (R), of width  $w_L = w_R \sim 2 \, \mu m$ , amplitude  $\delta n_L(t=0) = \delta n_R(t=0) \simeq 16 \, \mu m^{-1}$ , moving at a speed  $v_L = v_R = 1.9 \, \mu m/ms$ . The former values of  $\delta n_{L,R}$  correspond to a density perturbation of about 20% of the linear density  $n_{1D} = 78 \, \mu m^{-1}$ .

To achieve perturbation amplitudes larger than 20%, we employ a third experimental scheme. The first two approaches were limited by the generation of higher-order momentum excitations: in the former, ramping the potential to substantially higher or lower values, and in the latter, significantly increasing the edge shift, both led to rapid dispersion of the wave packet. In the new scheme, the system is initially prepared in a box potential feauturing a small central dimple, followed by a sudden quench to a flat box potential. After the quench, the dimple splits into two wave packets that propagate symmetrically from the center toward the edges of the system with opposite velocities. Varying the initial dimple size allows precise control over the resulting perturbation amplitude. A typical experiment is shown in Fig. 1(c). Each wave packet has a width  $w_L = w_R \sim 3 \,\mu m$  and travels at speed  $v_L = v_R = 1.8 \, \mu m/ms$ ; Four milliseconds after the quench, their amplitude is  $\delta n_L(t=4) = \delta n_R(t=4) = 27 \,\mu m^{-1}$ , corresponding to 39% of the linear density  $n_{1D} = 68 \ \mu m^{-1}$ .

The latter two protocols are implemented by replacing the opaque mask with a digital micromirror device (DMD) which enables arbitrary shaping of the longitudinal potential (for more details refer to section A of SM). Using the DMD offers the advantage of compensating for the residual shallow harmonic potential generated by the chip [31], where the quasicondensate is prepared, thereby improving the symmetry and

homogeneity of the system. We notice indeed that, the population of odd modes in the two experiment realized with DMD is overall smaller than in the low-amplitude experiment. In general, non-resonant mode populations arise primarily from thermal fluctuations, with small contributions from potential asymmetries. Finite phonon lifetimes broaden the resonance lines,  $\Delta\omega\sim\Gamma_k$ , explaining the weak excitation of non-resonant modes—such as the sixth harmonic during eighth-mode driving—consistent with nonlinear mode mixing. Systematic linewidth spectroscopy would offer a direct probe of phonon–phonon interactions, complementing the lifetime measurements presented here.

The extracted damping for the ensemble of modes excited through wave packet initiation is shown in panel (a) of Fig. 3. Here we plot the normalized damping  $\Gamma$  as a function of  $\tilde{k}$ , for each of the three experiments: low-amplitude perturbations (magenta), and stronger perturbations induced by edge displacement (orange) and dimple quench (green). The corresponding initial temperature is  $T_r = 40(4) nK$ ,  $T_{s}=60\,(6)\,\mathrm{nK}$  and  $T_{d}=69\,(5)\,nK$ , where  $r,\,s,$  and d label the ramp, edge-shift, and dimple experiments, respectively. Due to the finite system size and the imaging resolution, only a limited number of modes is accessible, in the given range of linear density  $(70 - 80 \,\mu\text{m}^{-1})$ . Therefore, the collected data do not form a Gaussian statistical distribution, thus preventing a meaningful fit. Instead, we directly compare the measurements with the theoretical damping expression of Eq. 1 (black line), where we have chosen  $\alpha = 0.76$ , as obtained from the single mode analysis (Fig. 2(a)). Interestingly, the observed damping at weak perturbation reproduces the behaviour predicted by Andreev's hydrodynamic theory, with

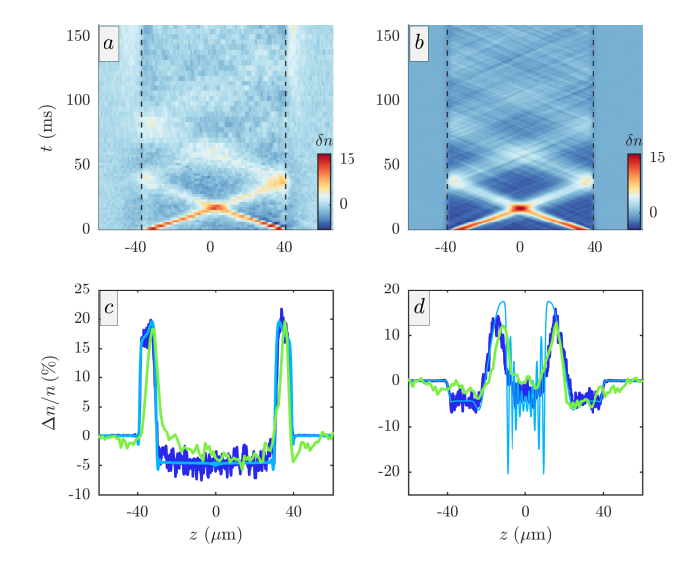


FIG. 4. Comparison between NPSE simulations and experimental data of a large amplitude wave packet. Panel a): experimental data for the evolution of a density perturbation which is about 20% of the linear density  $n_{1D}=70\,\mu\mathrm{m}^{-1}$ . Panel b): NPSE simulations at  $T=65\,\mathrm{nK}$ . Panel c) and d): density perturbation profiles  $\Delta n/n$  at t=0 (left) and t=10 (right). Experimental profile is plotted in green, in dark blue is the profile obtained via finite temperature NPSE simulations and in light blue is the profile obtained with the same experimental parameter, but at zero temperature. At  $t=10\,\mathrm{ms}$  fast oscillations are present in the zero-temperature profile, indicating that a wave-breaking phenomena has occoured, but thermal fluctuations cover the high-frequency oscillations.

the previously found coefficient, while it significantly deviates from it for stronger perturbations. A more detailed analysis to ensure statistical significance to our measurements is provided in section C of the Supplemental material. Additionally, in Fig. 3(a) we compare experimental data to numerical simulations (shaded area) obtained by solving the non-polynomial Schrödinger equation (NPSE) [20]: The agreement is consistent across all regimes, suggesting that while phonon decay is the predominant process at weak perturbations, the nonlinear behaviour at strong perturbations originates from a different mechanism.

To investigate the dynamics of the 1D quasi-condensate when the wave packet amplitude represents at least the 15% of the linear density, we provide, in Fig. 4 a more detailed comparison between experiment and numerical simulations. We consider the dynamics of the wave packet obtained via edge displacement, whose perturbation amplitude is about 20% of  $n_{1D}$ , and we find that the observed dynamics is in excellent agreement with the simulated data (Fig. 4(a,b)).

To gain more insight about the underlying physics, we look at the profile of the density perturbation at two distinct times, t=0 which sets the end of the walls displacement and  $t=10\,ms$ . In both cases, we find a perfect overlap between the experimental profile (green line) and the NPSE data (dark blue line). In addition to finite temperature NPSE numerical simulation, we consider NPSE simulations at zero temperature (light blue line) and compare them to experimental data:

while the agreement at t=0 is still good, after  $10\,ms$  we notice that the zero-temperature profile features fast oscillations, suggesting that a wave-breaking process has occourred [32, 33].

This phenomenon is a consequence of the velocity gradient  $\Delta c = c_p - c_b$  between the base  $(c_b)$  and the peak  $(c_p)$  of the propagating wave packet. This leads to a deformation of the wave packet, the peak moving faster than the base. Whenever  $\Delta c \cdot t$  becomes of the order of the characteristic size of the wave packet  $(\sigma_{wp})$  a shock wave forms. For  $\frac{\Delta n}{n} \ll 1$   $\Delta c = \frac{dc}{dn} \Delta n = \frac{c}{2} \frac{\Delta n}{n}$  and the typical timescale for wave braking  $t_{wb}$  can be estimated as

$$t_{wb}^{-1} \approx \frac{c}{2\sigma_{wp}} \left(\frac{\Delta n}{n}\right).$$
 (3)

For the wave packets shown in Fig. 4a), with  $\Delta n/n \sim 20\%$ ,  $c=1.9~\mu \text{m/ms}$  and  $\sigma_{wp}\equiv w_{R/L}\approx 2~\mu m$ , we estimate  $t_{wb}\approx 10~\text{ms}$ , which is significantly shorter than the experimentally observed evolution time and, although roughly estimated, is consistent with numerical results (Fig. 4(d)). Notably, wave breaking is expected to occur even for weak perturbations, albeit on much longer timescales. Due to its nature, the wave-breaking mechanism occours at both zero and finite temperatures. However, at finite temperature, thermal fluctuations wash out the high frequency oscillation, thus making them experimentally unaccessible. Nevertheless, as demonstrated here, this effect is evident in the coherent dynamics, where the observed mode damping deviates from the  $k^{3/2}$  behaviour, as seen in Fig. 3(a).

We have achieved the first direct observation of phonon decay driven by microscopic phonon–phonon scattering in a 1D Bose gas, thereby accessing a universal regime in the finite-temperature, low-momentum limit. By selectively exciting individual phononic modes, we revealed the characteristic  $k^{3/2}$  scaling of the damping rate in quantitative agreement with Andreev's hydrodynamic prediction. For stronger perturbations involving collective wave packets, we observed a clear deviation from this universal behavior, consistent with wave-breaking dynamics. Finite-temperature NPSE simulations corroborated these findings and enabled the separation of phonon–phonon scattering from highly nonlinear effects.

Looking forward, interferometric measurements of connected higher-order phase correlations [34, 35] would enable direct access to phonon–phonon vertices, while multimode resolution may allow exploration of the crossover from hydrodynamic damping to nonlinear Luttinger-liquid lineshapes. Our results thus establish a quantitative benchmark and a roadmap for the controlled study of relaxation and integrability breaking in quantum many-body systems, bridging fundamental theory and experimental quantum simulation.

We thank T. Schweigler and B. Rauer for helping with the initial experimental setup and E. Demler and M. Michael for helpful discussions. This research was support by the DFG / FWF under the Collaborative Research Center SFB 1225 ISOQUANT (Project-ID 27381115, Austrian Science Fund

(FWF) I 4863) and the the European Research Council: ERC-AdG "Emergence in Quantum Physics" (EmQ) under Grant Agreement No. 101097858. and by the Austrian Science Fund (FWF) [Grant No. I6276, QuFT-Lab].

- \* Present address: Division of Biology and Biological Engineering, California Institute of Technology, Pasadena, CA, USA
- [1] M. Girardeau, "Relationship between systems of impenetrable bosons and fermions in one dimension," J. Math. Phys. 1, 516–523 (1960).
- [2] E. H. Lieb and W. Liniger, "Exact analysis of an interacting Bose gas. I. The general solution and the ground state," Phys. Rev. 130, 1605 (1963).
- [3] E. H. Lieb, "Exact analysis of an interacting Bose gas. II. The excitation spectrum," Phys. Rev. **130**, 1616–1624 (1963).
- [4] F. D. M. Haldane, "Effective harmonic-fluid approach to lowenergy properties of one-dimensional quantum fluids," Phys. Rev. Lett. 47, 1840–1843 (1981).
- [5] T. Giamarchi, *Quantum physics in one dimension* (Clarendon press, Oxford, 2003).
- [6] M. A. Cazalilla, "Bosonizing one-dimensional cold atomic gases," Journal of Physics B: Atomic, Molecular and Optical Physics 37, S1 (2004).
- [7] M. A. Cazalilla, R. Citro, T. Giamarchi, E. Orignac, and M. Rigol, "One dimensional bosons: From condensed matter systems to ultracold gases," Rev. Mod. Phys. 83, 1405–1466 (2011).
- [8] A. Imambekov, T.L. Schmidt, and L.I. Glazman, "One-dimensional quantum liquids: Beyond the luttinger liquid paradigm," Reviews of Modern Physics 84, 1253–1306 (2012).
- [9] Benjamin Doyon, Sarang Gopalakrishnan, Frederik Møller, Jörg Schmiedmayer, and Romain Vasseur, "Generalized hydrodynamics: A perspective," Phys. Rev. X 15, 010501 (2025).
- [10] T. Kinoshita, T. Wenger, and D. S. Weiss, "A quantum Newton's cradle," Nature 440, 900–903 (2006).
- [11] M. Gring, T. Langen, M. Kuhnert, T. Kitagawa, M. Schreitl, I. Mazets, D. Smith, E. Demler, and J. Schmiedmayer, "Relaxation and Prethermalization in an Isolated Quantum System," Science 337, 1318–1322 (2012).
- [12] B. Rauer, S. Erne, T. Schweigler, F. Cataldini, M. Tajik, and J. Schmiedmayer, "Recurrences in an isolated quantum manybody system," Science 360, 307–310 (2018).
- [13] Y. Tang, W. Kao, K.-Y. Li, S. Seo, K. Mallayya, M. Rigol, S. Gopalakrishnan, and B. L. Lev, "Thermalization near integrability in a dipolar quantum Newton's cradle," Phys. Rev. X 8, 021030 (2018).
- [14] K. V. Samokhin, "Lifetime of excitations in a clean Luttinger liquid," Journal of Physics: Condensed Matter 10, L533 (1998).
- [15] A. Imambekov and L.I. Glazman, "Universal theory of nonlinear Luttinger liquids," Science **323**, 228–231 (2009).
- [16] A. F. Andreev, "The hydrodynamics of two-and one-dimensional liquids," Soviet Phys. JETP **51**, 1038 (1980).
- [17] Christophe Mora and Yvan Castin, "Extension of Bogoliubov theory to quasicondensates," Phys. Rev. A 67, 053615 (2003).
- [18] I. E. Mazets, T. Schumm, and J. Schmiedmayer, "Breakdown of integrability in a quasi-1D ultracold bosonic gas," Phys. Rev. Lett. 100, 210403 (2008).
- [19] Shina Tan, M. Pustilnik, and L.I. Glazman, "Relaxation of a high-energy quasiparticle in a one-dimensional Bose gas," Phys. Rev. Lett. 105, 090404 (2010).

- [20] L. Salasnich, A. Parola, and L. Reatto, "Effective wave equations for the dynamics of cigar-shaped and disk-shaped Bose condensates," Phys. Rev. A 65, 043614 (2002).
- [21] V. E. Zakharov and A. B. Shabat, "Interaction between solitons in a stable medium," Sov. Phys. JETP 37, 823–828 (1973).
- [22] P. Grisins and I. E. Mazets, "Thermalization in a onedimensional integrable system," Phys. Rev. A 84, 053635 (2011).
- [23] S. Hofferberth, I. Lesanovsky, B. Fischer, T. Schumm, and J. Schmiedmayer, "Non-equilibrium coherence dynamics in one-dimensional bose gases," Nature 449, 324–327 (2007).
- [24] A. A. Burkov, M. D. Lukin, and Eugene Demler, "Decoherence dynamics in low-dimensional cold atom interferometers," Phys. Rev. Lett. 98, 200404 (2007).
- [25] H.-P. Stimming, N. J. Mauser, J. Schmiedmayer, and I. E. Mazets, "Dephasing in coherently split quasicondensates," Phys. Rev. A 83, 023618 (2011).
- [26] J. Reichel and V. Vuletić, Atom Chips (Wiley-VCH, Weinheim, Germany, 2011).
- [27] P. Krüger, S. Hofferberth, I. E. Mazets, I. Lesanovsky, and J. Schmiedmayer, "Weakly interacting bose gas in the onedimensional limit," Physical Review Letters 105, 265302 (2010).
- [28] F. Cataldini, F. Møller, M. Tajik, J. Sabino, Si-Cong Ji, I. Mazets, T. Schweigler, B. Rauer, and J. Schmiedmayer, "Emergent pauli blocking in a weakly interacting bose gas," Phys. Rev. X 12, 041032 (2022).
- [29] P. C. Hohenberg and P. C. Martin, "Microscopic theory of superfluid helium," Ann. Phys. (N.Y.) 34, 291–359 (1965).
- [30] P. Szépfalusy and I. Kondor, "On the dynamics of continuous phase transitions," Ann. Phys. (N.Y.) 82, 1–53 (1974).
- [31] M. Tajik, B. Rauer, T. Schweigler, F. Cataldini, J. Sabino, F.S. Møller, Si-Cong Ji, I.E. Mazets, and J. Schmiedmayer, "Designing arbitrary one-dimensional potentials on an atom chip," Opt. Express 27, 33474–33487 (2019).
- [32] S. A. Simmons, F. A. Bayocboc, J. C. Pillay, D. Colas, I. P. McCulloch, and K. V. Kheruntsyan, "What is a quantum shock wave?" Phys. Rev. Lett. 125, 180401 (2020).
- [33] Philipp Schüttelkopf, Mohammadamin Tajik, Nataliia Bazhan, Federica Cataldini, Si-Cong Ji, Jörg Schmiedmayer, and Frederik Møller, "Characterising transport in a quantum gas by measuring drude weights," (2024), arXiv:2406.17569 [cond-mat.quant-gas].
- [34] T. Schweigler, V. Kasper, S. Erne, I.E. Mazets, B. Rauer, F. Cataldini, T. Langen, T. Gasenzer, J. Berges, and J. Schmiedmayer, "Experimental characterization of a quantum manybody system via higher-order correlations," Nature 545, 323– 326 (2017).
- [35] T.V. Zache, T. Schweigler, S. Erne, J. Schmiedmayer, and J. Berges, "Extracting the field theory description of a quantum many-body system from experimental data," Physical Review X 10, 011020 (2020), arXiv:1909.12815 [cond-mat.quant-gas].
- [36] Bernhard Rauer, *Non-equilibrium dynamics beyond dephasing:* Recurrences and loss induced cooling in one-dimensional Bose gases (Springer, Heidelberg, 2019).
- [37] S. Manz, R. Bücker, T. Betz, Ch. Koller, S. Hofferberth, I. E. Mazets, A. Imambekov, E. Demler, A. Perrin, J. Schmiedmayer, and T. Schumm, "Two-point density correlations of quasicondensates in free expansion," Phys. Rev. A 81, 031610 (2010).
- [38] Thomas Schweigler, "Correlations and dynamics of tunnel-coupled one-dimensional bose gases," (2019).

#### SUPPLEMENTAL MATERIAL

# Preparation of the initial state

Our quasicondensate of <sup>87</sup>Rb atoms is realized following standard protocols of magneto-optical trapping, laser cooling, and evaporative cooling to bring the system to the degeneracy temperature. The atom chip generates a rf-dressed cigarshaped magnetic trap in which the final stage of evaporative cooling is performed [36]. The frequency in the two tight transverse directions is fixed, but slightly changed over time due to setup upgrade and optimization. In all the weak perturbation experiments  $\omega_{\perp} = 2\pi \times 1.27$  kHz, while for the medium to strong perturbation experiments  $\omega_{\perp} \simeq 2\pi \cdot 1.38$ kHz. On the other hand, the frequency in the elongated direction is the same for all the data presented  $\omega_{\parallel} \simeq 2\pi \cdot 7$  Hz. The geometry of the trap in the longitudinal direction can be modified by overimposing to one of the two transverse directions of the magnetic trap a blue-detuned dipole potential. The box-like shape is achieved using two different methods, either by shining the blue-detuned laser light onto an opaque mask [12, 36], or onto a digital micromirror device (DMD) [28, 31]. The total number of atoms in the initial state can be tuned by adjusting the evaporative cooling radio-frequency.

Box confinement using an opaque mask - The box trap employed in the single-mode excitation experiments (Fig. 2) and small-amplitude wavepacket measurements (Fig. 3(b)) is realized by using a blue-detuned laser light of wavelength 767 nm. To create the box, the laser light is shined onto a wired mask with opaque stripes of varying widths. The transversely aligned Gaussian beam, blocked at its centre by the selected stripe, generates a potential that adds two steep walls to the shallow harmonic magnetic confinement. In these experiments, the box length is  $L\sim49\,\mu\mathrm{m}$ , with wall widths  $w_{L/R}\simeq2.5\,\mu\mathrm{m}$ . Owing to the small box size relative to the longitudinal potential, the curvature of the bottom of the trap can be neglected.

Box confinement using a DMD - The wave packet protocols based on the DMD are shown in Fig. 3(c,d). In these experiments, the laser light employed to produce the box trap has a wavelength 660 nm. The DMD compensates for the harmonic curvature of the bottom of the trap, and provides the submicron accuracy, with a projected pixel size of  $0.417~\mu m$  in the plane of the atoms. Each trap geometry is obtained through an iterative optimization of the DMD mask against the measured density profile. Due to experimental limitations, the box walls acquire a finite width; fitting the density with error functions yields wall widths of  $2-4~\mu m$ .

### Out of equilibrium protocols

The thermal properties and dynamics of the system are probed through a large statistical set of absorption images after time-of-flight (ToF). Each data set usually includes 150-250 repetitions. The longitudinal density profile used to track

non-equilibrium dynamics is obtained from images taken after a short TOF of 2 ms, while the total atom number and temperature are extracted from density ripples appearing after 11.2 ms of ToF [37, 38]. During the dynamics of our Bose gas, the heating of the system is negligible, and the measured atom loss rate ranges between 0.5 and 2 atoms/ms; it arises from three-body recombination, collisions with the background gas particles, and technical noise.

#### Single mode excitation

The generic  $j^{\text{th}}$  phononic mode is excited by continuously modulating the intensity of the blue-detuned laser light at frequency  $\nu_{k_j} = (2\pi)^{-1} c k_j = c \frac{j}{2L}$ , where c is the speed of sound and L is the box length. The modulation is generated through an arbitrary waveform generator as  $V(-\tau_{dr} \leq$  $t \leq 0$  =  $V_0 + V_{\epsilon} \cos(2\pi\nu_{k_i})$ , with  $\tau_{dr}$  the driving time. This protocol is particularly suited for small perturbation amplitudes  $V_{\epsilon}$ , as stronger modulations cause heating and nonnegligible loss of atoms from the box, thus affecting c. The dynamics is probed through the density perturbation  $\delta n(z,t)$ , as defined in the main text, which quantifies the coherent population of the addressed mode. The excitation of the lowest symmetric mode is shown in Fig. 1(a), while the three next higher modes are shown in Fig. 5. We consider relatively short shaking times,  $\tau_{dr} = [30, 60]$  ms. Driving the system for only a few oscillations limits unwanted heating and minimizes integrability-breaking processes such as three-body loss.

## Wave packets after fast ramp

A schematic of the protocol is illustrated in the panel at the bottom of Fig. 6. The system, initially prepared in the potential  $V_0$  is ramped down in  $t_R = 1$  ms to the final value  $V_f$ . The small change in the position of the box walls creates a depletion of atoms which begins to propagate from the edges inward, at the speed of sound  $c = 1.7 \,\mu\text{m/ms}$ . In the middle box, the full longitudinal density profile of the atomic cloud n(z) is shown at selected times: the thermal initial state is shown with a yellow line and the first four time steps after the quench are shown with a blue gradient, the dark blue representing the beginning of the free evolution after the quench (t = 0). Although the change in potential is barely noticeable in the full density profile as extracted from ToF pictures, the propagation of the perturbation becomes evident when the background profile  $\langle n(z) \rangle_t$  is removed. In the upper panel of Fig. 6 we show  $\delta n(z) = n(z) - \langle n(z) \rangle_t$ at t = 0 (dark blue line) and in the following three time steps (shown in different shades of blue). Although small, the peaks of the wave pakets are now clear. The complete evolution carpet is shown in Fig. 1b) of the main text, where the dynamics has been recorded for 100 ms, and its relative mode decomposition is plotted in Fig. 3(b).

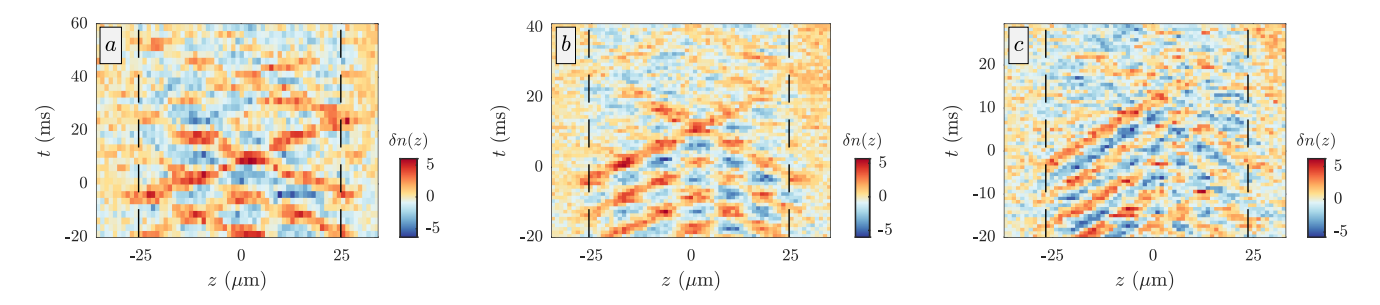


FIG. 5. Excitation of higher order phononic modes. The  $4^{\rm th}$ ,  $6^{\rm th}$  and  $8^{\rm th}$  modes are addressed in panel (a), (b) and (c) respectively. Each 2D plot shows the evolution of the density perturbation profile  $\delta n(z,t)$  during the last 20 ms of shaking (negative times) and for the full subsequent evolution. The lifetime of the mode noticibly decreases for higher order modes. The dashed black lines represent the position of the box walls which is used in the computation of the Fourier decomposition (see Fig. 2(b-e))

### Box edge displacement

Starting from a box potential of length L, both walls are shifted in n small steps of size  $\Delta z$ , and duration  $\Delta t$ , until it reaches the final box length  $L_s$ . This is achieved by sequentially turning on pixels rows of the DMD. During the translation of the box wall, a momentum is imprinted onto the atoms at the edge of the box and the propagation of a wave packet is initiated on each side, (Fig.7).

The bottom frame of Fig.7 schematically represents a measurement where the box length is reduced in  $\Delta t=5$  ms, by turning on one pixel row every millisecond - corresponding to  $\Delta z\approx 0.4\,\mu\mathrm{m}$  - yielding a total displacement of  $\Delta L\approx 2\,\mu\mathrm{m}$  per wall, thus reducing the length of the box from  $L=82\,\mu\mathrm{m}$  to  $L_s=78\,\mu\mathrm{m}$ . The quasi-condensate is initially prepared in a thermal state at temperature T=60(6) nK and has a linear density of  $n_{1D}=78\,\mu\mathrm{m}^{-1}$ . The evolution of the density

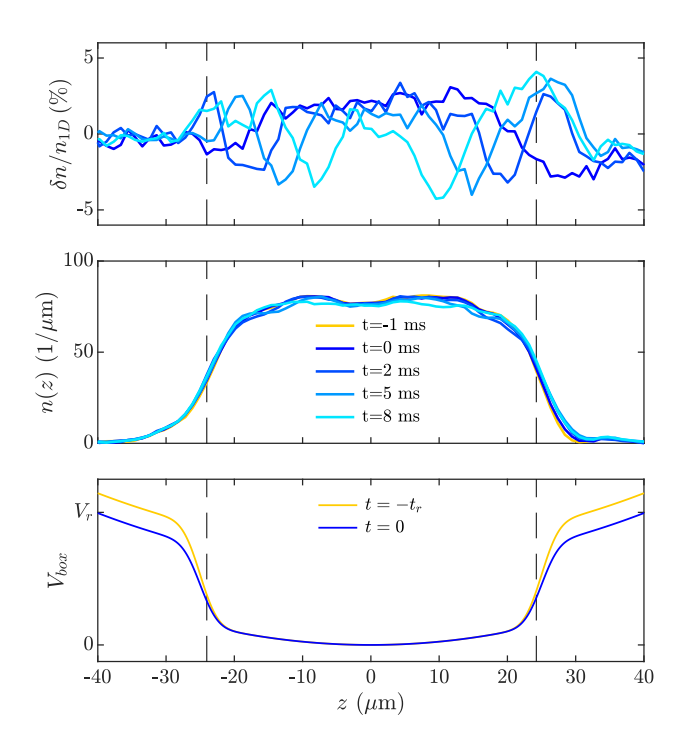


FIG. 6. Quench in the potential. Top: The density perturbation profile  $\delta n(z)/n_{1D}$  is plotted for selected times, t=0,2.5,5,7.5 ms and shown with different shades of blue, the darker corresponding to t=0. Middle: The full density profile n(z) is shown for the same time steps as in the top panel. Additionally, the density profile for the thermal state is plotted with a yellow line. Bottom: Schematic of the experimental protocol, with  $V_r$  representing the final potential amplitude. In all the three panels, the black dashed lines indicate the position of the walls of the box.

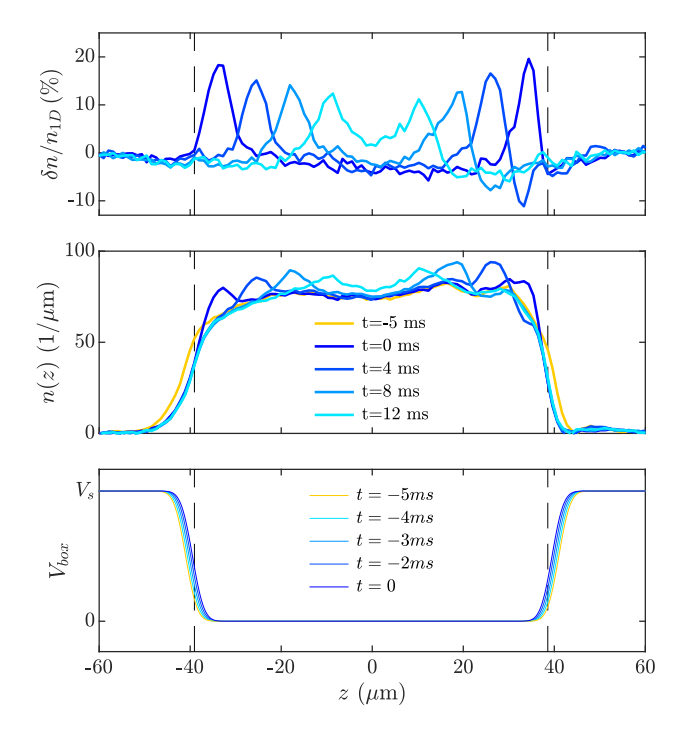


FIG. 7. **Edge displacement protocol.** Top: The density perturbation profile  $\delta n(z)/n_{1D}$  is plotted for selected times, t=0,4,8,12 ms and shown with different shades of blue, the darker corresponding to t=0. Middle: The full density profile n(z) is shown for the same time steps as in the top panel. Additionally, the density profile for the thermal state is plotted with a yellow line. Bottom: Schematic of the experimental protocol: in yellow is shown the potential at thermal state  $(t=-5\,\mathrm{ms})$  and in dark blue the final potential (t=0). The intermediate potentials are shown in gradients. In all the three panels, the black dashed lines indicate the position of the walls of the box.

perturbation  $\delta n(z)$  is shown, for a few initial times in the top frame of Fig. 7, while the full dynamics is plotted in Fig. 4a) of the main text. In all the frames of Fig.7 the vertical dashed lines represent the position of the edges of the box at t=0.

#### Quench from dimple to flat box potential

A schematic of the protocol is illustrated in the panel at the bottom of Fig. 8. The initial state is prepared in a box potential of length  $L_d=103\,\mu\mathrm{m}$ , featuring a small dimple in the middle. For the measurement presented in Fig. 8, the dimple has a width if  $\sigma = 4 \,\mu\text{m}$ , while the initial temperature is T=69(5) nK and the linear density  $n_{1D}=68~\mu\mathrm{m}^{-1}$ . The initial potential is suddenly quenched to a flat box potential, having same length  $L_d$ . Following the quench, the dimple splits into two wave-pakets, propagating from the middle to the edges of the box at speed  $c = 1.8 \,\mu\text{m/ms}$ . The top and central panel of Fig. 8 show the density perturbation  $\delta n(z)$ and and the full density profile n(z) respectively, during the first 16 ms of evolution after the quench, in steps of 4 ms. The thermal state at  $t = -\delta t$  is plotted in yellow. The full dynamics is plotted in Fig. 1(c) of the main text. The position of the box walls is marked by dashed vertical lines in all the

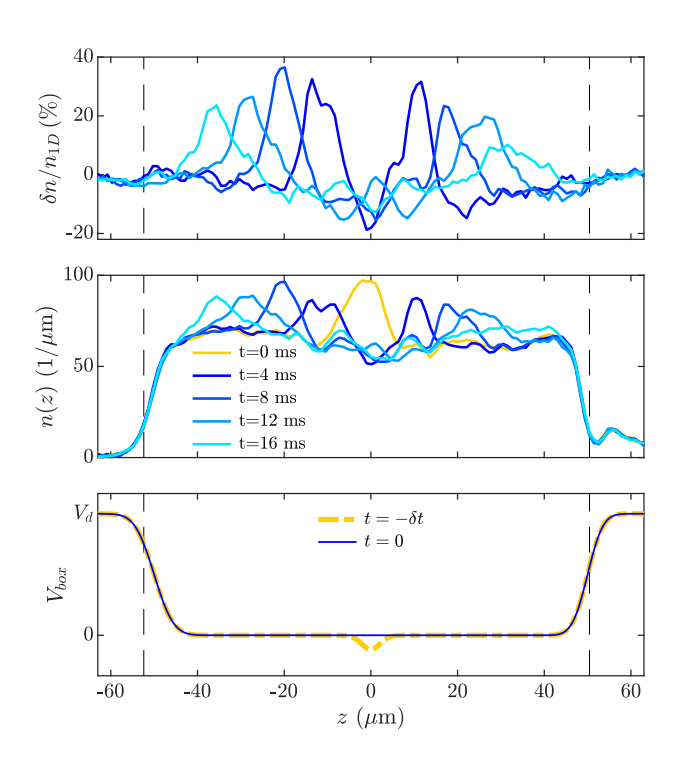


FIG. 8. **Dimple protocol.** Top: The density perturbation profile  $\delta n(z)/n_{1D}$  is plotted for selected times, the initial time  $t=-\delta t$  is in yellow, while the evolution times t=4,8,12,16 ms are shown with different shades of blue, the darker corresponding to t=0. Middle: The full density profile n(z) is shows for the same time steps as in the top panel. Bottom: Schematic of the experimental protocol, where in yellow is shown the potential in the thermal state and in dark blue the flat potential it is quenched to. In all the three panels, the black dashed lines indicate the position of the walls of the box.

panels.

#### Methods

## Power-law modeling of the damping rate

The behaviour of the normalized damping rate  $\tilde{\Gamma}(\tilde{k})$ , with  $\tilde{\Gamma} = \frac{m}{\hbar} \frac{\lambda_1^4}{4} \Gamma$  and  $\tilde{k} = \frac{\lambda_T}{2}$ , extracted from single mode excitation (Fig. 2) is modeled using a power-law function of the form  $y = \alpha x^{\beta}$ . To linearize this model, both variables are log-transformed, giving  $\log(y) = \log(\alpha) + \beta \log(x)$ . A linear regression is then performed in log space, with centering applied to the predictor variable to improve numerical stability and to reduce correlations. The fitted slope  $\beta$  represents the scaling exponent, while the intercept corresponds to  $\log(\alpha)$ , allowing estimation of the original parameters in the power-law relationship. The estimated parameters in the original  $(\tilde{\Gamma}, \tilde{k})$ -space are  $\beta = 1.48 \, (0.03)$  and  $\alpha = 0.76 \, (0.02)$ , with uncertainties that give the standard deviations derived from the covariance matrix of the fit.

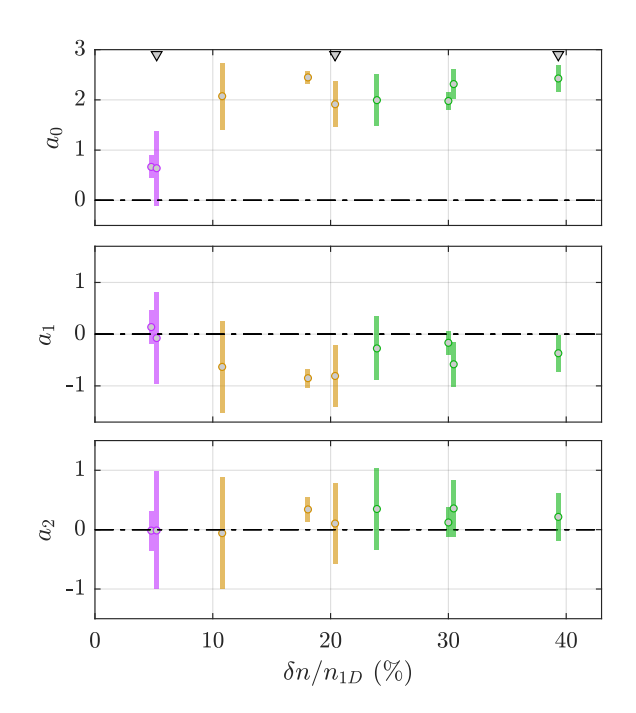


FIG. 9. Polynomial regression on wave packets measurements. The ratio  $\Theta = \Gamma/\Gamma_{th}$ , with  $\Gamma$  and  $\Gamma_{th}$  the measured and predicted damping rate, is fitted with a third-order Legendre polynomials  $f = a_0 P_0 + a_1 P_1 + a_2 P_2$ . The statistical significance of the coefficients  $a_0$   $a_1$  and  $a_2$  is evaluated via polynomial regression. The errors on the coefficients are obtained from the fit. In magenta: data sets corresponding to ramp/up of the box potential; in orage: edge displacement measurements; in green: dimple quenched to a flat box potential. The three grey arrows on top mark the data sets shown in the main text. The measurements have  $n_{1D} \in [66, 86] \, \mu m^{-1}$ ,  $T \in [40, 70] \, nK$ .

To assess the agreement between the damping rate measured via wave packet excitations  $\Gamma$ , shown in Fig. 3, and the theoretical prediction  $\Gamma_{th} = \sqrt{(k_B T)/(m n_{1D})} k^{3/2}$ , we perform polynomial regression analysis on the ratio  $\Theta(k) =$  $\Gamma(k)/\Gamma_{th}(k)$ . We fit  $\Theta$  with  $f = a_0 P_0(\xi) + a_1 P_1(\xi) +$  $a_2P_2(\xi)$ , where  $P_0, P_1, P_2$  are the zeroth, first and second order Legendre polynomials respectively, defined with respect to the center of the k-axis,  $\xi = (k - k)/\Delta k$ , with  $\bar{k}=(k_{min}+k_{max})/2$  and  $\Delta k=k_{max}-\bar{k}$ , and evaluate the statistical significance of the coefficients  $a_0$ ,  $a_1$ ,  $a_2$ . The zeroth-order coefficient  $a_0$  represents a uniform scaling factor between experimental data and theory, while the higher-order coefficients,  $a_1 a_2$ , capture systematic deviations as a function of  $\xi$ . In addition to the three data sets analyzed in Fig. 3, we perform a regression analysis on additional measurements where we excite wave packets with varying perturbation amplitude,  $\delta n/n_{1D} \in [0.05, 0.4]$ . The results are plotted in Fig. 9. Here, we show the fitted coefficients  $a_0$ ,  $a_1$ ,  $a_2$  with relative errorbars. Data points with distinct colors correspond to different kinds of protocol: magenta for ramp up/down of the potential, orange for box edge displacement, and green for dimple quenched to a flat box. The data presented in Fig. 3 of the main text, are here highlighted by grey arrows at the top of the figure. For small perturbation measurements,  $a_1, a_2 \approx 0$ and only the zeroth-order coefficient  $a_0$  is statistically significant, proving that  $\Theta$  is constant and that the experimental data agree with the theoretical model. Additionally, the scaling factor close to 0.7, is consistent with the coefficient  $\alpha = 0.76$ obtained by fitting the shaking measurements damping rate (Fig. 2). For perturbation amplitude  $\delta n/n_{1D} \geq 16\%$ , the higher-order coefficients  $a_1$ ,  $a_2$  are statistically significant, indicating a deviation from Andreev's prediction.

## Theoretical background

An ultracold 1D gas made of bosons with mass m, chemical potential  $\mu$ , trapped in a longitudinal potential U(z) is described, in mean-field approximation, by the Hamiltonian:

$$H = \int dz \, \psi^{\dagger} \left[ -\frac{\hbar^2}{2m} \partial_z + U - \mu + \frac{g_{1D}}{2} \psi^{\dagger} \psi \right] \psi, \quad (4)$$

where z is the longitudinal direction of the gas,  $g_{1D}$  is the 1D coupling constant characterizing the interparticle interaction, here assumed to occur via a  $\delta$ -function. For repulsive interactions  $g_{1D}>0$ . The Hamiltonian 4 without the term containing U(z) and  $\mu$  is the Lieb-Liniger Hamiltonian [2]. For brevity, the dependence on z has been removed,  $\psi^{\dagger}(z) \equiv \psi^{\dagger}$ ,  $\psi(z) \equiv \psi$ . The Bogoliubov theory can be extended to 1D systems [17], in phase-density representation, assuming the wavefunction to be expressed as  $\psi(z,t) = \sqrt{\rho(z,t)}\,e^{i\theta(z,t)}$ , where  $\rho$  and  $\theta$  represent the local density and the phase of the quasicondensate respectively. After expanding the density

around a uniform background  $\rho(z,t)=\rho_0+\delta\rho(z,t)$  and assuming small density fluctuations  $\delta\rho(z,t)\ll |\rho_0|$ , H can be expanded in terms of the phase  $\theta$  and the density fluctuations  $\delta n$ :  $H=H_1+H_2+H_3+\ldots$  The Hamiltonian H reduces to

$$H \sim \int dz \left[ \frac{\hbar^2 \rho_0}{2m} (\partial_z \theta)^2 + \frac{g_{1D}}{2} (\delta \rho)^2 + \frac{\hbar^2}{8m\rho_0} (\partial_z \delta \rho)^2 + \frac{\hbar^2}{2m} \delta \rho (\partial_z \theta)^2 - \frac{\hbar^2}{8m\rho_0} \delta \rho (\partial_z \delta \rho)^2 \right].$$
(5)

In the former equation, the first two quadratic terms represent the Luttinger-liquid Hamiltonian, which does not capture the full long-time scale dynamics of a weakly-interacting 1D Bose gas out of equilibrium [12, 28]. The third term in eq. 5 is the quantum pressure, and the last two terms represent, respectively, the phonon-phonon interaction and the density fluctuations self-interaction. In the phononic regime, dominated by long-wavelength excitations, the Bogoliubov dispersion relation becomes linear, and the leading interaction is the phonon-phonon scattering. For  $\omega=c|k|$  and at low k, Andreev has derived the power-low decay for the damping of phonons  $\Gamma \propto k^{3/2}$  [16] In this regime the quantum pressure term is also negligible, while it is responsible for the wavebreaking mechanisms occourring for larger perturbations.

#### Comparison to nonlinear Luttinger liquids

The seminal book by Giamarchi [5] provides the foundational framework of one-dimensional quantum systems through bosonization and Luttinger liquid theory, where excitations are strictly stable due to the assumption of a linearized dispersion. Within this paradigm, correlation functions display universal algebraic behavior but phonons remain infinitely long-lived. The role of band curvature and other irrelevant operators is acknowledged, yet only as perturbative corrections within the renormalization group language, without a quantitative description of phonon lifetimes. Subsequent developments went beyond this framework: Samokhin [14] showed that dispersion curvature leads to finite lifetimes of excitations, while the nonlinear Luttinger liquid (NLL) theory of Imambekov and Glazman [15] established a universal description of dynamical response functions in the presence of nonlinearity, predicting the replacement of  $\delta$ -peaks by powerlaw edge singularities.

Whereas Andreev's self-consistent hydrodynamic approach predicts a finite phonon lifetime with the non-analytic scaling law  $\Gamma_k \propto T^{1/2} k^{3/2}$  [16], the nonlinear Luttinger liquid (NLL) framework developed by Imambekov and Glazman [15] arrives at a qualitatively different picture. In the linear Luttinger model, phonons are strictly stable and appear as  $\delta$ -function peaks in dynamical response functions. The inclusion of dispersion curvature, however, removes this protection: in the NLL theory the sharp  $\delta$ -peaks are replaced by universal

power-law edge singularities at the exact Lieb-Liniger excitation thresholds. Thus, rather than acquiring a simple exponential damping rate, phonons in the NLL picture manifest as broadened, asymmetric continua in  $S(k,\omega)$  and  $A(k,\omega)$ . Our measurements directly probe the low-k, finite-temperature hy-

drodynamic regime where Andreev's law is valid, while extensions toward higher-momentum or higher-energy excitations would connect to the universal non-Lorentzian lineshapes predicted by the NLL theory.